NANO LETTERS

pubs.acs.org/NanoLett Letter

Strong Coupling in All-Dielectric Intersubband Polaritonic Metasurfaces

Raktim Sarma,* Nishant Nookala, Kevin James Reilly, Sheng Liu, Domenico de Ceglia, Luca Carletti, Michael D. Goldflam, Salvatore Campione, Keshab Sapkota, Huck Green, George T. Wang, John Klem, Michael B. Sinclair, Mikhail A. Belkin, and Igal Brener*

Cite This: *Nano Lett.* 2021, 21, 367−374 Read Online

ACCESS | Metrics & More | Article Recommendations | Supporting Information

ABSTRACT: Mie-resonant dielectric metasurfaces are excellent candidates for both fundamental studies related to light−matter interactions and for numerous applications ranging from holography to sensing to nonlinear optics. To date, however, most applications using Mie metasurfaces utilize only weak light-matter interaction. Here, we go beyond the weak coupling regime and demonstrate for the first time strong polaritonic coupling between Mie photonic modes and intersubband (ISB) transitions in semiconductor heterostructures. Furthermore, along with demonstrating ISB polaritons with Rabi splitting as large as 10%, we also demonstrate the ability to tailor the strength of strong coupling by engineering either the semiconductor heterostructure or the photonic mode of the resonators. Unlike previous plasmonic-based works, our new all-dielectric metasurface approach to generate ISB polaritons is free from ohmic losses and has high optical damage thresholds, thereby making it ideal for creating novel and compact mid-infrared light sources based on nonlinear optics.

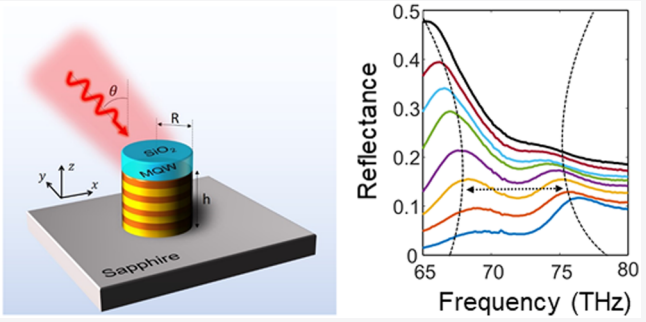

KEYWORDS: *strong light−matter interaction, polaritons, III−V semiconductors, intersubband transitions, dielectric metasurfaces*

Metasurfaces, which are the planar equivalents of metamaterials, have attracted significant attention as platforms for fundamental studies related to light−matter interaction and for numerous applications.[1] Broadly speaking, metasurfaces can be classified as either plasmonic or all-dielectric, where the former consists of an array of metal-dielectric nanoresonators and the latter utilizes meta-atoms that are fabricated out of high refractive index dielectric materials.[1,2]

Although metal nanoresonators have the advantage of being subwavelength in size, they are intrinsically lossy at optical wavelengths and have low optical damage thresholds, which prohibits many applications at technologically relevant wavelengths. Additionally, metal nanoresonators tend to enhance electromagnetic fields only near the surface of the metallic elements,[3] which limits the ability to control the interaction volume and tailor light−matter interactions at the nanoscale. On the other hand, dielectric resonators exhibit extremely low loss and high damage thresholds. They support Mie-type volume resonances where a major portion of the electromagnetic fields is confined within the volume of the resonator.[2,3] The field distribution of the Mie modes can be controlled using the symmetry, shape, and size of the dielectric resonators. Because of their design flexibility, low optical losses, and high damage thresholds, all-dielectric metasurfaces have recently been explored for numerous applications ranging from imaging[4,5] and holography[6] to ultrathin nonlinear optical elements.[7−9]

Most of metasurfaces demonstrated to date produce tailored optical response by electromagnetic engineering of optical modes in nanoresonators. Recently, more complex *polaritonic* metasurface designs that exploit polaritonic coupling of optical intersubband (ISB) transitions in multiquantum-well (MQW) semiconductor heterostructures and optical modes in nanoresonators[10,11] were proposed and experimentally demonstrated. This novel design approach has already resulted in metasurfaces with unique functionalities such as record-high second-order nonlinear optical response,[12−15] optical power limiters,[16] and mid-infrared detectors with record detectivity.[17] All these structures were based on polaritonic coupling of intersubband transitions of MQWs with optical modes of metal nanoresonators. However, as mentioned earlier, metasurfaces based on metal resonators have several disadvantages compared

Received: September 16, 2020
Revised: December 8, 2020
Published: December 21, 2020

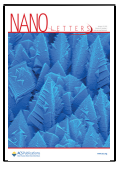

https://dx.doi.org/10.1021/acs.nanolett.0c03744
Nano Lett. 2021, 21, 367−374

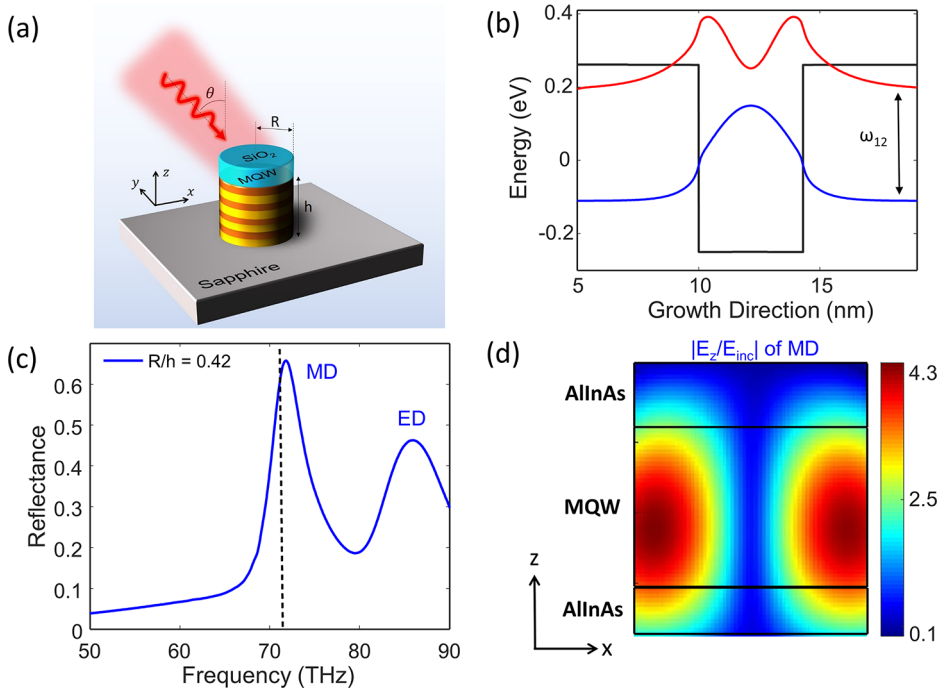

Figure 1. Schematic and working principle of the dielectric intersubband polaritonic metasurface. (a) Schematic of the metasurface unit cell. The height (h) of all the fabricated cylindrical Mie resonators is 1.25 μm. The radii (R) of the cylinders are varied to vary the spectral position of the magnetic dipole (MD) Mie resonances. (b) 8 band k.p band structure calculation of the conduction band of a single period of the MQW heterostructure used in this study. The quantum well thickness is designed to support a single intersubband transition at the transition frequency $\omega_{12}/(2\pi) \approx 71$ THz. The layer sequence of the single period of the heterostructure is 10 nm/4.3 nm/10 nm, where the thicknesses of the $Al_{0.52}In_{0.48}As$ barrier is shown in bold and the $In_{0.53}Ga_{0.47}As$ well is in normal font. The $In_{0.53}Ga_{0.47}As$ layer is uniformly n-doped and electron density averaged over the entire MQW region is 1.4×10^{17} cm^{-3}. (c) Finite-difference-time-domain calculations of the reflectance spectrum from an optimized metasurface comprised of cylinders with $R/h = 0.42$ with electric field polarized along x and incidence angle $\theta = 15°$. The MD resonance is spectrally aligned with the intersubband transition frequency which is shown by the black dashed line (d) Finite-difference-time domain simulation results of the MD mode in the nanoresonator in c. Shown is the absolute value of the z-component of the electric field in the central plane of the nanoresonator normalized with respect to incident field E_{inc}.

to all-dielectric metasurfaces. In this work, we demonstrate for the first time ISB polaritonic metasurfaces with all-dielectric nanoresonators and show that these structures can be designed to operate in the strong-coupling regime. Low losses and high optical damage threshold of all-dielectric metasurfaces are expected to be particularly important for nonlinear optics where high intensity pump beams are used.

In our nanoscale all-dielectric polaritonic system, the light component of the strongly interacting system corresponds to the Mie photonic modes of the dielectric resonators, while the matter component comprises electronic ISB transitions of semiconductor quantum wells (QWs) embedded within the dielectric nanoresonators. In addition to demonstrating strong coupling, we also show that the light−matter coupling strength in the dielectric metasurface can be tailored by engineering either the matter excitation or the photonic mode through the geometry of the nanoresonator.

The strength of light−matter coupling depends on both the nature of the matter excitation as well as the fields of the photonic mode. In the strong-coupling regime, the light−matter coupling strength dominates over the losses of the system. This regime leads to the formation of new hybrid eigenstates called polaritons which are a superposition of a photonic mode and a matter excitation.[10,11,18] The minimum energy separation between the two polariton branches in the frequency domain is called Rabi splitting (in the time domain, this is observed as a Rabi oscillation).[10,11,19] Although many systems can demonstrate strong coupling,[10,11,20−27] very few offer the flexibility to independently tailor both the light and matter components of the light−matter interaction. In this letter, we demonstrate that all-dielectric metasurfaces indeed offer such a flexible platform. To do this, we present our results in two parts. In the first part, we concentrate on the matter aspect of the light−matter interaction and study ISB polaritons in metasurfaces that support the same photonic Mie resonance but are coupled to different semiconductor heterostructures. This part focuses on engineering the matter excitation by controlling the number of electrons in the strongly coupled system. In the second part, we focus on the photonic aspect and study ISB polaritons in metasurfaces that utilize the same semiconductor heterostructure but are coupled to different photonic Mie resonances. This part focuses on leveraging different photonic mode profiles supported by the resonators to tailor the strength of the light−matter coupling.

Figure 1a shows a schematic of a meta-atom of the polaritonic dielectric metasurface that was experimentally investigated. The metasurface consists of periodically spaced cylindrical dielectric resonators fabricated from III−V semiconductors with n-doped $In_{0.53}Ga_{0.47}As/Al_{0.52}In_{0.48}As$ MQWs (see Methods for fabrication details). The semiconductor resonators are bonded to a sapphire substrate and are capped by an SiO_2 layer. Both SiO_2 and sapphire have a much lower refractive index (∼1.4 and ∼1.76, respectively) than that of the MQW heterostructure (∼3.3). This refractive index contrast is the key to allow the meta-atoms to host highly confined Mie-type photonic modes with resonant frequencies that can be spectrally tuned by

https://dx.doi.org/10.1021/acs.nanolett.0c03744
Nano Lett. 2021, 21, 367−374

controlling the radius (R) and height (h) of the cylinders. The MQW heterostructure embedded within the resonators is optimized to support a single ISB transition at $\omega_{12}/(2\pi)$ = 71 THz (4.2 μm). Figure 1b shows an 8-band k.p band structure calculation of a single period of the MQW system used in this study. The heterostructure has $Al_{0.52}In_{0.48}As$ layers in the top and bottom and in the center is made of multiple repetitions of $Al_{0.52}In_{0.48}As$ and $In_{0.53}Ga_{0.47}As/Al_{0.52}In_{0.48}As$ layers. The heterostructures are grown by the molecular beam epitaxy (MBE) on an InP substrate. The details of the MQW structure and fabrication methods are given in Methods.

Strong coupling of the photonic mode to the ISB transitions requires the fulfilment of the two conditions: (1) the resonant frequencies of the photonic mode and the ISB transition should spectrally align and (2) the photonic mode should have significant electric field components normal to the QW multilayer interfaces in order to satisfy the ISB selection rules.[28]

For the first part of the study, we chose to spectrally overlap the ISB transition with the lowest-order dipole Mie resonance, i.e., the resonance associated with magnetic dipole (MD) mode. For a fixed wavelength (corresponding to the ISB transition) and fixed height of the cylindrical resonator, the first Mie mode that we observe for the smallest radii of the cylindrical resonators is the MD mode.[29] At that wavelength, the other higher-order modes can be supported only by resonators of larger radii. Choosing the MD mode, therefore, allows for the smallest achievable resonator dimensions. We varied R to spectrally align the MD mode with the ISB transition. Figure 1c shows a numerically calculated reflectance spectrum of the optimized metasurface, which shows that for cylinders of dimensionless scale factor, R/h = 0.42, the MD resonance spectrally aligns with the ISB transition. We keep h fixed at 1.25 μm in this study. Choosing the MD mode also allows us to satisfy the second condition mentioned above, since this mode creates strong z-directed electric field components (due to its circulating out-of-plane electric fields). Figure 1d shows numerically calculated absolute values of the z-directed electric field E_z normalized to the incident field E_{inc} in the $x-z$ plane at the center of the resonator, for the MD resonance shown in Figure 1c at a frequency of 71 THz. Having fulfilled both requirements for strong coupling, we then proceeded to investigate the formation of ISB polaritons and study their dependence on the matter excitation in two different polaritonic metasurface systems.

The dependence of Rabi splitting of the ISB polaritons on the matter excitation can usually be well understood by the Dicke Model which predicts that for a given photonic mode, an increase of the electron density inside the resonator enhances the light-matter coupling, and the Rabi splitting ($\Delta\omega_R$) scales as $\sqrt{N_e}$ where N_e is the total number of electrons inside the resonator.[11,30−32] To confirm this prediction for all-dielectric metasurfaces, we fabricated and measured two types of metasurfaces. For both metasurfaces, the resonators have the same size and shape (therefore they support the same MD mode) but they are integrated with two different heterostructures. The two heterostructures have the same thicknesses of the $Al_{0.52}In_{0.48}As/In_{0.53}Ga_{0.47}As/Al_{0.52}In_{0.48}As$ layers (10 nm/4.3 nm/10 nm) and therefore same ISB resonant frequency, $\omega_{12}/(2\pi)$ = 71 THz but have different number of QWs and different doping levels, and therefore different N_e. The first heterostructure (W_1) has N_1^{QW} = 30 QWs with doping density (N_1^d) = 8×10^{17} cm^{-3} in the quantum well. The electron density averaged over the entire MQW region (N_1^v) for W_1 is therefore = 1.4×10^{17} cm^{-3}. The second heterostructure (W_2) has N_2^{QW} = 40 QWs with doping density of N_2^d = 3×10^{18} cm^{-3} in the quantum well and the average electron density of N_2^v= 5.3×10^{17} cm^{-3}. Based on the prediction of Dicke's model, the ratio of Rabi splitting for these two samples should be $\sim \sqrt{\frac{4N_2^v}{3N_1^v}}$ = 2.2. Because the thicknesses of the QWs are the same for both W_1 and W_2, increasing N_d and N_{QW} should only change the number of participating electrons and for these doping densities, to first order, not the ISB resonance frequency itself.[33,34] We confirmed this by performing normalized FTIR transmission measurements of the bare samples in a waveguide configuration (details in Methods). Figure 2a shows the measured transmission

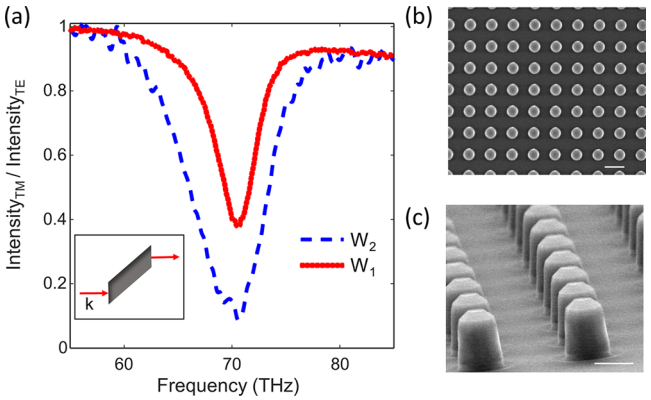

Figure 2. Characterization of the MQW heterostructures and fabricated metasurfaces. (a) Experimentally measured intersubband absorption spectrum of the two MQW heterostructures used in this study. The inset shows the configuration used for the absorption measurements with the input direction indicated. The absorption spectrum is produced by taking the ratio of the intensity of the transmitted transverse magnetic polarized input light to the intensity of the transmitted transverse electric polarized input light. (b, c) Top and side view scanning electron micrographs of one of the fabricated metasurfaces. The white scale bar corresponds to 2 μm (1 μm) in b (c).

spectra, and we clearly see that both samples have the same ISB resonance frequency (corresponding to the minima in transmission spectra). Increasing N_d and N_{QW} only increases the amplitude and the line width of the ISB absorption feature in the spectrum.

To demonstrate the dependence of the Rabi splitting $\Delta\omega_R$ on N_e, we fabricated and measured three sets of metasurfaces. Figure 2b, c show scanning electron micrographs of one of the fabricated samples. We started with a control sample, where the metasurfaces contained embedded W_2 heterostructure but the cylinders had relatively large radii so that all the metasurfaces had the scale factors R/h much larger than 0.42. Because in these structures, the MD resonance (at ~62 THz) is spectrally detuned from the ISB resonance, we do not expect to observe any spectral signature of light−matter coupling between the Mie mode and the ISB. Furthermore, small changes of the nanoresonator radii should lead to a linear spectral scaling of the MD resonance. Figure 3a shows the experimentally measured reflectance spectra of the metasurfaces. As expected, no coupling is observed, and we measure a linear scaling of the MD resonance with increasing the nanoresonator radii. Next, we measured our polaritonic metasurfaces with cylinders of varying radii and with scale factors R/h centered around 0.42 to sweep the bare cavity resonance across the ISB transition. Figure 3b, c

https://dx.doi.org/10.1021/acs.nanolett.0c03744
Nano Lett. 2021, 21, 367−374

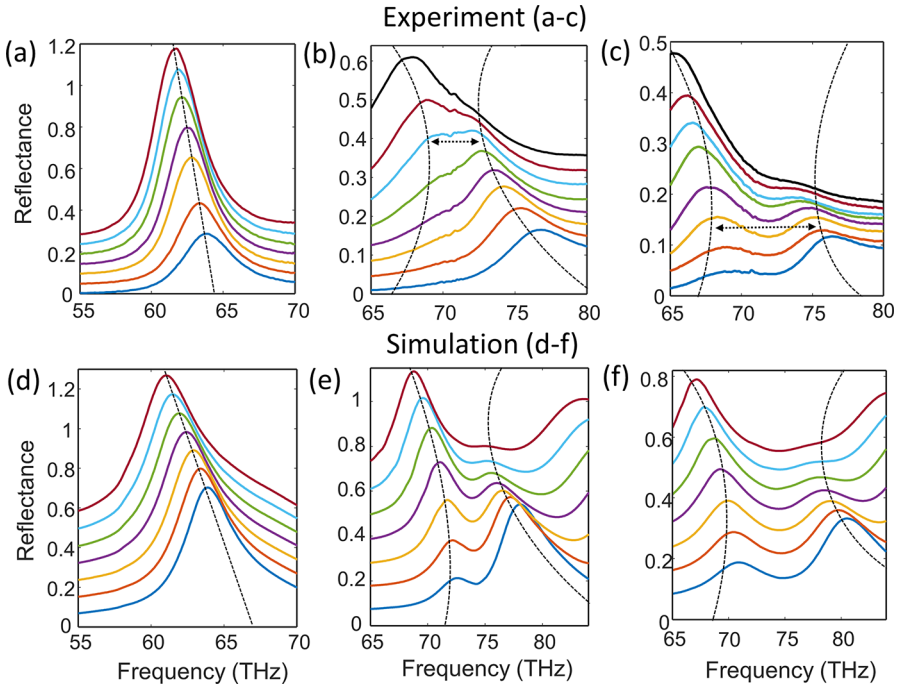

Figure 3. Experimental and numerical simulation spectra of the metasurfaces with the magnetic dipole (MD) resonance coupled to ISB transitions. (a) Experimentally measured reflectance spectra of the metasurfaces made of resonators of different radii with the MD resonances detuned from the ISB transition resonance. The scale factor of the cylinders (R/h) varies from 0.52 to 0.59 in equal steps with the curve at the top corresponding to the largest scale factor/radius. Reflectance curves are offset vertically for clarity. Small changes to the radii lead to linear spectral scaling of the MD resonance. (b, c) Experimentally measured reflectance spectra of the metasurfaces with resonators of different radii with the MD resonances spectrally overlapping with the ISB resonance supported by (b) W_1 and (c) W_2 heterostructures, respectively. The scale factor of the cylinders (R/h) varies from 0.4 to 0.49 in equal steps with the curve at the top corresponding to the largest scale factor/radius. Reflectance curves are offset vertically for clarity. A clear anticrossing behavior of the polariton branches is observed. The double-sided arrows in (b,c) correspond to experimentally measured Rabi splitting $\Delta\omega_R$. (d) Numerically calculated reflectance spectra of the metasurfaces made of the resonators of different radii with the MD resonances detuned from ISB resonance. The scale factor of the cylinders (R/h) varies from 0.5 to 0.55 in equal steps with the curve at the top corresponding to the largest scale factor/radius. Reflectance curves are offset vertically for clarity. (e, f) Numerically calculated reflectance spectra of the metasurface with resonators of different radii with the MD resonances spectrally overlapping with the ISB resonance supported by (e) W_1 and (f) W_2 heterostructures, respectively. The scale factor of the cylinders (R/h) varies from 0.39 to 0.44 in equal steps with the curve at the top corresponding to the largest scale factor/radius. A good agreement with experiments is observed. In all panels, the dashed lines are shown as guide to eyes.

shows the experimental results for two different sets of metasurfaces loaded with W_1 and W_2 heterostructures, respectively (see Methods for the details of the experimental measurements). As opposed to linear scaling, in both cases, one can now see the anticrossing of the two polariton branches. Furthermore, for the metasurfaces loaded with the heterostructure W_2 (Figure 3c), the magnitude of the Rabi splitting $\Delta\omega_R/\omega_{12} \approx 10\%$ of the center frequency and is about 2 times larger compared to the metasurfaces loaded with W_1 heterostructure for which $\Delta\omega_R/\omega_{12} \approx 5\%$. These results nicely follow the predictions of Dicke's model and in turn demonstrate the ability to tailor light-matter interactions in these dielectric metasurfaces by engineering the matter excitation independently of the photonic resonance. To validate our experimental results, we also analytically calculated the polariton dispersion and compared the calculated values with our experimental values. We get excellent agreement, and the calculations are shown in the Supporting Information. We also point out here that the Rabi splitting of ~10% is comparable to what has been observed using intersubband polaritonic metasurfaces with metal nanoresonators[19,31] and it is also comparable to the generally considered threshold for transitions to the ultrastrong coupling regime.[30] Finally, to verify the experimental results, we performed finite-difference time domain numerical simulations of all the three cases corresponding to the structures in Figure 3a–c (see Methods for the details of simulations). Figure 3d–f shows the simulation results, which are in good qualitative agreement with the experiment.

Unlike plasmonic metasurfaces, where the field polarization is perpendicular to metal layers and the fields decay rapidly away from metal, in dielectric metasurfaces, the types of Mie modes supported by a metasurface, along with their corresponding polarization and spatial mode profiles, can be varied by adjusting the shape, size, or symmetry of the resonators comprising the metasurface. Our ability to engineer the polarization and the spatial mode profile of a Mie resonator provides an additional degree of freedom that can be leveraged to tailor the strength of the light–matter coupling. To investigate this photonic aspect of light–matter interaction in the dielectric metasurfaces, we studied metasurfaces that are loaded with the same semiconductor heterostructure but support different types of Mie modes. As a proof-of-concept, we chose the simplest case of comparing the polaritonic splitting for electric dipole (ED) mode and the MD mode in the nanoresonators.

We fabricated two sets of metasurfaces using a third semiconductor heterostructure design W_3 with $N_3^{QW} = 30$ QWs, $N_3^{d} = 3 \times 10^{18}$ cm^{-3}, and $N_3^{v} = 5.3 \times 10^{17}$ cm^{-3}. The design of a single period of the MQW and the ISB transition frequency of the W_3 heterostructure is the same as for W_1 and W_2. In the first set of metasurfaces fabricated from the W_3

https://dx.doi.org/10.1021/acs.nanolett.0c03744
Nano Lett. 2021, 21, 367–374

heterostructure, we fabricated cylinders of varying radii and with scale factors R/h centered around 0.42 so that the MD resonance couples to the ISB transition. In the second set of metasurfaces, we fabricated cylinders of varying radii with larger scale factors R/h centered around 0.58 such that the cylinders now support an out-of-plane electric dipole (ED) Mie mode centered at around 71 THz (Figure 4a). Instead of the most

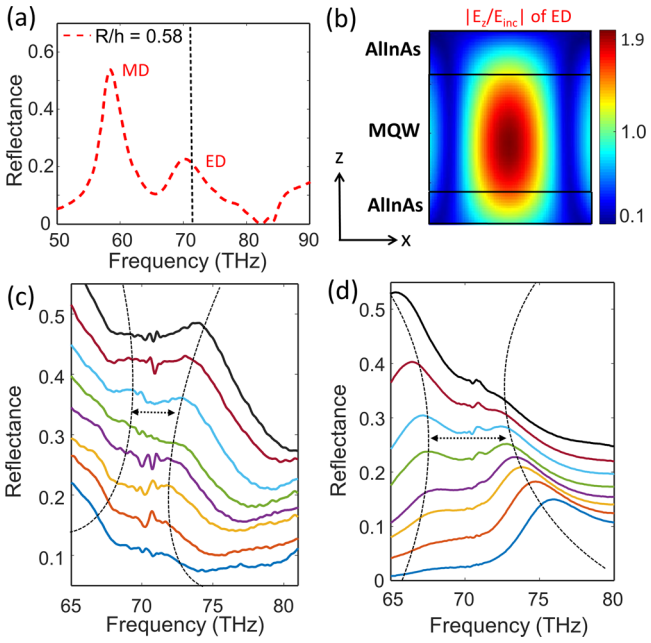

Figure 4. Comparison of strong coupling of electric dipole (ED) resonance and MD resonance to intersubband transitions. (a) Finite-difference-time-domain calculations of reflectance from an optimized metasurface with cylinders of $R/h = 0.58$ at an incidence angle $\theta = 15°$. The out-of-plane ED resonance spectrally aligns with the intersubband transition shown by the black dashed line. Because of the off-normal incidence condition, the electric field is polarized in the $x-z$ plane which allows us to excite the ED mode easily. (b) Finite-difference-time domain calculation of absolute value of z-directed electric field E_z normalized to incident field E_{inc} in the $x-z$ plane at the center of the resonator for the ED resonance at 71 THz shown in a. (c, d) Experimentally measured reflectance spectrum of resonators of different radii with (c) ED and (d) MD resonances spectrally overlapping with the ISB resonance supported by W_3 heterostructure. For (c) the ED resonance, the scale factor of the cylinders (R/h) varies from 0.56 to 0.65 in equal steps and for (d) MD resonance, the scale factor of the cylinders (R/h) varies from 0.4 to 0.49. Reflectance curves are offset vertically for clarity with the curve at the top corresponding to the largest scale factor/radii. The dashed lines are shown as guides to the eye. In comparison to (d) the MD resonance, a much smaller and less pronounced Rabi splitting $\Delta\omega_R$ (shown by the double sided arrows) is observed for (c) the ED resonance. The experimental measurements were done using a FTIR microscope fitted with a Schwarzschild objective of numerical aperture = 0.4, so that the samples were illuminated at off-normal incidence angles ($8° < \theta < 23°$), which allowed us to excite the out-of-plane ED resonance.

commonly used in-plane ED mode, we chose the out-of-plane ED mode as it has a nonzero z component of electric field which is required to couple to the ISB transition. This mode can be coupled to using off-normal incidence (see Methods). Figure 4b shows numerically calculated absolute values of the electric field E_z normalized with respect to the incident field E_{inc} in the $x-z$ plane at the center and inside the resonator for the ED resonance shown in Figure 4a.

From Figure 4b, we clearly see that the spatial distribution (and therefore the spatial overlap between the z-directed electric fields and the multi-QWs) of $|E_z|$ of the ED mode is different than that for the MD mode shown in Figure 1d. This indicates that the strength of light−matter coupling in the metasurface that supports the MD resonance should be different compared to the metasurface that supports the ED resonance. To confirm this prediction, we experimentally measured the reflectance spectra of both metasurfaces which are presented in Figure 4c, d. Indeed, a more pronounced and larger Rabi splitting is observed for the metasurfaces that support the MD resonance which has larger spatial overlap of $|E_z|$ with the multi-QWs in comparison to the metasurfaces that support the ED resonance. This demonstrates that in these polaritonic all-dielectric metasurfaces, the light-matter interaction can be tailored by engineering the photonic resonance that couples to the matter excitation. Finally, we also performed numerical simulations of the coupling of the ED mode to the intersubband transition. The simulation results are shown in the Supporting Information and they are in good qualitative agreement with the experimental results in Figure 4.

In summary, we have fabricated and characterized the first all-dielectric ISB polaritonic metasurfaces comprising of electromagnetically engineered dielectric nanoresonators loaded with semiconductor heterostructures with quantum-engineered ISB transitions. We exploited the two lowest order dipole Mie modes supported by the dielectric resonators to strongly couple to the intersubband transitions. Using our all-dielectric metasurface platform, we demonstrated the ability to tailor the strength of the light-matter interaction and realize polaritons with variable Rabi splitting by either engineering the semiconductor heterostructure (the matter) or by coupling the ISB transitions to different photonic modes of the nanoresonator (the light). This all-dielectric nanoresonator design approach allows one to avoid ohmic losses intrinsic to metasurface with metal-based nanoresonator designs, while providing similar coupling strengths to intersubband transitions. All-dielectric ISB polaritonic metasurfaces can therefore have potential use in creating new ultrathin classical and quantum light sources using nonlinear wave phenomena such as high harmonic generation or quantum optical process such as parametric down conversion in the mid-infrared spectral region (often referred to as the "molecular fingerprint" region of the electromagnetic spectrum). Such light sources will be of paramount importance for spectroscopy, sensing, and imaging applications where there is currently a lack of compact mid-infrared light sources which are robust, mobile, and require low power.

METHODS

Sample Fabrication. The heterostructure had $Al_{0.52}In_{0.48}As$ layers in the top and bottom and in the center was comprised of n-doped $In_{0.53}Ga_{0.47}As/Al_{0.52}In_{0.48}As$ multi-QW heterostructure (described in Figure 1b). The entire heterostructure was first grown on a semi-insulating InP substrate using molecular beam epitaxy. For samples with different number of QWs, the thicknesses of $Al_{0.52}In_{0.48}As$ layers were varied to ensure that the height (h) of the resonators is fixed at 1.25 μm. The wafer was then flipped and bonded to a Sapphire substrate. After bonding, the InP substrate was removed to transfer the epitaxial $Al_{0.52}In_{0.48}As$ and $In_{0.53}Ga_{0.47}As/Al_{0.52}In_{0.48}As$ QW layers to the Sapphire substrate. The final step involved e-beam lithography and inductively coupled plasma reactive ion etching for defining and fabricating the cylinders. The lower refractive index SiO_2

https://dx.doi.org/10.1021/acs.nanolett.0c03744
Nano Lett. 2021, 21, 367−374

layer on top of the cylinders was used as the mask for the dry etching.

Experimental Measurements. The semiconductor heterostructures (W_1, W_2, and W_3) were optically characterized using a Fourier-transform infrared spectroscopy (FTIR) setup. As shown in the inset of Figure 2a, the bare wafers were polished to have 45 deg input and output facets and ISB transition resonant frequencies and line widths were determined by taking the ratio of transmission of transverse magnetic polarized normal incident input light to transverse electric polarized input light. The input direction (k) of the incident light used for the measurements is shown in the inset of Figure 2a. The reflectance from the fabricated metasurfaces was measured using a FTIR microscope fitted with a Schwarzschild objective of numerical aperture = 0.4, so that the samples were illuminated at off-normal incidence angles $8° < \theta < 23°$ (see Figure 1a). The off-normal incidence allowed us to excite the out-of-plane ED resonance which, unlike the MD resonance, cannot be excited by normal incident illumination of the samples.

Numerical Simulations. The reflectance spectra of the polaritonic metasurfaces were calculated using a commercially available finite-difference-time domain solver (Lumerical). The multi-QW was modeled as a homogeneous, anisotropic layer with dielectric-constant tensor $\boldsymbol{\epsilon}_{QW} = \epsilon_t(\hat{x}\hat{x} + \hat{y}\hat{y}) + \epsilon_l\hat{z}\hat{z}$, where the transverse dielectric constant is $\epsilon_t = 11.08$ and the longitudinal dielectric constant is $\epsilon_l = 11.08 + \frac{f_{12}\omega_{12}^2}{\omega_{12}^2 - \omega^2 - 2i\omega\gamma_{12}}$.

In the above, the Lorentzian term models the optical transition at 71 THz. The resonant angular frequency, $\omega_{12} = 2\pi \times 71 \times 10^{12}$ rad/s, of the ISB transition is same for all the three samples (W_1, W_2, and W_3) used in this study. The term $2\gamma_{12}$ represents the ISB transition damping rate due to the resonant absorption (note each sample exhibits a different loss parameter that was determined by experimental measurements). The oscillator strength, f_{12} is also different for each sample and is proportional to the product of the doping density of the quantum wells and the dipole matrix length $z_{12} = 1.24$ nm between the electronic level 1 and level 2. The dipole matrix lengths, ISB resonant frequency, and band structures shown in Figure 1b were determined from calculations using *NextNano3*, a commercial software by nextnano GmbH. To consider the periodicity of the resonators and off-normal incidence condition, we solved the electromagnetic problem using finite-difference-time-domain using broadband fixed angle source technique. For all the simulations, the angle of incidence was fixed at 15° with an electric field polarized along the x direction.

■ ASSOCIATED CONTENT

Supporting Information

The Supporting Information is available free of charge at https://pubs.acs.org/doi/10.1021/acs.nanolett.0c03744.

> Analytical calculations of polariton dispersion and comparison to experiments, calculation of spatial distribution of $|E_z|$ for different incident angles, numerical simulation of the ED mode as a function of scale factor, numerical simulation of the ED mode coupled to ISB transitions, and multipolar decomposition of the field profiles of the ED mode (PDF)

■ AUTHOR INFORMATION

Corresponding Authors

Raktim Sarma − *Sandia National Laboratories, Center for Integrated Nanotechnologies, Albuquerque, New Mexico 87123, United States;* orcid.org/0000-0002-7288-2044; Email: rsarma@sandia.gov

Igal Brener − *Sandia National Laboratories, Center for Integrated Nanotechnologies, Albuquerque, New Mexico 87123, United States;* orcid.org/0000-0002-2139-5182; Email: ibrener@sandia.gov

Authors

Nishant Nookala − *Department of Electrical and Computer Engineering, University of Texas at Austin, Austin, Texas 78712, United States*

Kevin James Reilly − *Department of Electrical and Computer Engineering, University of New Mexico, Albuquerque, New Mexico 87131, United States*

Sheng Liu − *Sandia National Laboratories, Albuquerque, New Mexico 87123, United States*

Domenico de Ceglia − *Department of Information Engineering, University of Padova, Padua 35122, Italy*

Luca Carletti − *Department of Information Engineering, University of Padova, Padua 35122, Italy;* orcid.org/0000-0001-6268-9817

Michael D. Goldflam − *Sandia National Laboratories, Albuquerque, New Mexico 87123, United States*

Salvatore Campione − *Sandia National Laboratories, Albuquerque, New Mexico 87123, United States;* orcid.org/0000-0003-4655-5485

Keshab Sapkota − *Sandia National Laboratories, Albuquerque, New Mexico 87123, United States*

Huck Green − *Sandia National Laboratories, Albuquerque, New Mexico 87123, United States*

George T. Wang − *Sandia National Laboratories, Albuquerque, New Mexico 87123, United States;* orcid.org/0000-0001-9007-0173

John Klem − *Sandia National Laboratories, Albuquerque, New Mexico 87123, United States*

Michael B. Sinclair − *Sandia National Laboratories, Albuquerque, New Mexico 87123, United States*

Mikhail A. Belkin − *Department of Electrical and Computer Engineering, University of Texas at Austin, Austin, Texas 78712, United States; Walter Schottky Institut, Technische Universitat Munchen, Garching 85748, Bavaria, Germany*

Complete contact information is available at: https://pubs.acs.org/10.1021/acs.nanolett.0c03744

Author Contributions

The manuscript was written through contributions of all authors. All authors have given approval to the final version of the manuscript.

Notes

The authors declare no competing financial interest.

■ ACKNOWLEDGMENTS

This work was supported by the U.S. Department of Energy, Office of Basic Energy Sciences, Division of Materials Sciences and Engineering and performed, in part, at the Center for Integrated Nanotechnologies, an Office of Science User Facility operated for the U.S. Department of Energy (DOE) Office of Science. Sandia National Laboratories is a multimission

laboratory managed and operated by National Technology and Engineering Solutions of Sandia, LLC, a wholly owned subsidiary of Honeywell International, Inc., for the U.S. Department of Energy's National Nuclear Security Administration under contract DE-NA0003525. The University of Texas group acknowledges financial support from the DARPA NASCENT program. This paper describes objective technical results and analysis. Any subjective views or opinions that might be expressed in the paper do not necessarily represent the views of the U.S. Department of Energy or the United States Government.

■ ABBREVIATIONS

ISB, intersubband; MQW, multiquantum-well; QW, quantum well; MBE, molecular beam epitaxy; MD, magnetic dipole; ED, electric dipole

■ REFERENCES

(1) Chen, H. T.; Taylor, A. J.; Yu, N. A Review of Metasurfaces: Physics and Applications. *Rep. Prog. Phys.* **2016**, *79* (7), No. 076401.
(2) Baranov, D. G.; Zuev, D. A.; Lepeshov, S. I.; Kotov, O. V.; Krasnok, A. E.; Evlyukhin, A. B.; Chichkov, B. N. All-Dielectric Nanophotonics: The Quest for Better Materials and Fabrication Techniques. *Optica* **2017**, *4* (7), 814−825.
(3) Krasnok, A.; Tymchenko, M.; Alu, A. Nonlinear Metasurfaces: A Paradigm Shift in Nonlinear Optics. *Mater. Today* **2018**, *21* (1), 8−21.
(4) Engelberg, J.; Zhou, C.; Mazurski, N.; Bar-David, J.; Kristensen, A.; Levy, U. Near-IR Wide-Field-of-View Huygens Metalens for Outdoor Imaging Applications. *Nanophotonics* **2020**, *9* (2), 361−370.
(5) Paniagua-Dominguez, R.; Yu, Y. F.; Khaidarov, E.; Choi, S.; Leong, V.; Bakker, R. M.; Liang, X.; Fu, Y. H.; Valuckas, V.; Krivitsky, L. A.; Kuznetsov, A. I. A Metalens with a Near-Unity Numerical Aperture. *Nano Lett.* **2018**, *18* (3), 2124−2132.
(6) Chong, K. E.; Wang, L.; Staude, I.; James, A. R.; Dominguez, J.; Liu, S.; Subramania, G. S.; Decker, M.; Neshev, D. N.; Brener, I.; Kivshar, Y. S. Efficient Polarization-Insensitive Complex Wavefront Control using Huygens' Metasurfaces based on Dielectric Resonant Meta-atoms. *ACS Photonics* **2016**, *3* (4), 514−519.
(7) Liu, S.; Sinclair, M. B.; Saravi, S.; Keeler, G. A.; Yang, Y.; Reno, J.; Peake, G. M.; Setzpfandt, F.; Staude, I.; Pertsch, T.; Brener, I. Resonantly Enhanced Second-Harmonic Generation Using III-V Semiconductor All-Dielectric Metasurfaces. *Nano Lett.* **2016**, *16* (9), 5426−5432.
(8) Camacho-Morales, R.; Rahmani, M.; Kruk, S.; Wang, L.; Xu, L.; Smirnova, D. A.; Solntsev, A. S.; Miroshnichenko, A.; Tan, H. H.; Karouta, F.; et al. Nonlinear Generation of Vector Beams from AlGaAs Nanoantennas. *Nano Lett.* **2016**, *16* (11), 7191−7197.
(9) Gili, V. F.; Carletti, L.; Locatelli, A.; Rocco, D.; Finazzi, M.; Ghirardini, L.; Favero, I.; Gomez, C.; Lemaitre, A.; Celebrano, M.; et al. Monolithic AlGaAs Second-Harmonic Nanoantennas. *Opt. Express* **2016**, *24* (14), 15965−15971.
(10) Dini, D.; Kohler, R.; Tredicucci, A.; Biasiol, G.; Sorba, L. Microcavity Polariton Splitting of Intersubband Transitions. *Phys. Rev. Lett.* **2003**, *90* (11), 116401.
(11) Jouy, P.; Vasanelli, A.; Todorov, Y.; Delteil, A.; Biasiol, G.; Sorba, L.; Sirtori, C. Transition from Strong to Ultrastrong Coupling Regime in Mid-infrared Metal-dielectric-metal Cavities. *Appl. Phys. Lett.* **2011**, *98*, 231114.
(12) Lee, J.; Tymchenko, M.; Argyropoulos, C.; Chen, P. Y.; Lu, F.; Demmerle, F.; Boehm, G.; Amann, M. C.; Alu, A.; Belkin, M. A. Giant Nonlinear Response from Plasmonic Metasurfaces Coupled to Intersubband Transitions. *Nature* **2014**, *511*, 65.
(13) Wolf, O.; Campione, S.; Benz, A.; Ravikumar, A. P.; Liu, S.; Luk, T. S.; Kadlec, E. A.; Shaner, E. A.; Klem, J. F.; Sinclair, M. B.; Brener, I. Phased-Array Sources Based on Nonlinear Metamaterial Nanocavities. *Nat. Commun.* **2015**, *6*, 7667.
(14) Lee, J.; Nookala, N.; Gomez-Diaz, J. S.; Tymchenko, M.; Demmerle, F.; Boehm, G.; Amann, M. C.; Alu, A.; Belkin, M. A. Ultrathin Second-Harmonic Metasurfaces with Record-High Nonlinear Optical Response. *Adv. Opt. Mater.* **2016**, *4* (5), 664−670.
(15) Nookala, N.; Xu, J.; Wolf, O.; March, S.; Sarma, R.; Bank, S.; Klem, J.; Brener, I.; Belkin, M. Mid-Infrared Second-Harmonic Generation in Ultra-thin Plasmonic Metasurfaces without a Full-Metal Backplane. *Appl. Phys. B: Lasers Opt.* **2018**, *124* (7), 124−132.
(16) Mann, S. A.; Nookala, N.; Johnson, S.; Mekkawy, A.; Klem, J. F.; Brener, I.; Raschke, M.; Alu, A.; Belkin, M. A. Ultrafast Optical Switching and Power Limiting in Intersubband Polaritonic Metasurfaces. In *OSA Technical Digest*; Optical Society of America: Washington, D.C., 2020; paper FTu4Q.7.
(17) Palaferri, D.; Todorov, Y.; Bigioli, A.; Mottaghizadeh, A.; Gacemi, D.; Calabrese, A.; Vasanelli, A.; Li, L.; Davies, A. G.; Linfield, E. H.; Kapsalidis, F.; Beck, M.; Faist, J.; Sirtori, C. Room-temperature Nine-μm-wavelength Photodetectors and GHz-frequency Heterodyne Receivers. *Nature* **2018**, *556* (7699), 85−88.
(18) Dovzhenko, D. S.; Ryabchuk, S. V.; Rakovich, Y. P.; Nabiev, I. R. Light−Matter Interaction in the Strong Coupling Regime: Configurations, Conditions, and Applications. *Nanoscale* **2018**, *10* (8), 3589−3605.
(19) Benz, A.; Campione, S.; Liu, S.; Montano, I.; Klem, J. F.; Allerman, A.; Wendt, J. R.; Sinclair, M. B.; Capolino, F.; Brener, I. Strong coupling in the sub-wavelength limit using metamaterial nanocavities. *Nat. Commun.* **2013**, *4* (1), 1−8.
(20) Yu, X.; Yuan, Y.; Xu, J.; Yong, K. T.; Qu, J.; Song, J. Strong Coupling in Microcavity Structures: Principle, Design, and Practical Application. *Laser & Photonics Reviews* **2019**, *13* (1), 1800219.
(21) Dintinger, J.; Klein, S.; Bustos, F.; Barnes, W. L.; Ebbesen, T. W. Strong Coupling Between Surface Plasmon-Polaritons and Organic Molecules in Subwavelength Hole Arrays. *Phys. Rev. B: Condens. Matter Mater. Phys.* **2005**, *71* (3), No. 035424.
(22) Bellessa, J.; Symonds, C.; Vynck, K.; Lemaitre, A.; Brioude, A.; Beaur, L.; Plenet, J. C.; Viste, P.; Felbacq, D.; Cambril, E.; Valvin, P. Giant Rabi Splitting between Localized Mixed Plasmon-Exciton States in a Two-Dimensional Array of Nanosize Metallic disks in an Organic Semiconductor. *Phys. Rev. B: Condens. Matter Mater. Phys.* **2009**, *80* (3), No. 033303.
(23) Scalari, G.; Maissen, C.; Turčinková, D.; Hagenmüller, D.; De Liberato, S.; Ciuti, C.; Reichl, C.; Schuh, D.; Wegscheider, W.; Beck, M.; Faist, J. Ultrastrong Coupling of the Cyclotron Transition of a 2D Electron Gas to a THz Metamaterial. *Science* **2012**, *335* (6074), 1323−1326.
(24) Shelton, D. J.; Brener, I.; Ginn, J. C.; Sinclair, M. B.; Peters, D. W.; Coffey, K. R.; Boreman, G. D. Strong Coupling between Nanoscale Metamaterials and Phonons. *Nano Lett.* **2011**, *11* (5), 2104−2108.
(25) Sarma, R.; Campione, S.; Goldflam, M.; Shank, J.; Noh, J.; Smith, S.; Ye, P. D.; Sinclair, M.; Klem, J.; Wendt, J.; et al. Low Dissipation Spectral Filtering using a Field-Effect Tunable III−V Hybrid Metasurface. *Appl. Phys. Lett.* **2018**, *113* (6), No. 061108.
(26) Jun, Y. C.; Reno, J.; Ribaudo, T.; Shaner, E.; Greffet, J. J.; Vassant, S.; Marquier, F.; Sinclair, M.; Brener, I. Epsilon-Near-Zero Strong Coupling in Metamaterial-Semiconductor Hybrid Structures. *Nano Lett.* **2013**, *13* (11), 5391−5396.
(27) Chen, Y.; Miao, S.; Wang, T.; Zhong, D.; Saxena, A.; Chow, C.; Whitehead, J.; Gerace, D.; Xu, X.; Shi, S. F.; Majumdar, A. Metasurface Integrated Monolayer Exciton Polariton. *Nano Lett.* **2020**, *20* (7), 5292−5300.
(28) West, L. C.; Eglash, S. J. First Observation of an Extremely Large-Dipole Infrared Transition Within the Conduction Band of a GaAs Quantum Qell. *Appl. Phys. Lett.* **1985**, *46* (12), 1156−1158.
(29) Staude, I.; Miroshnichenko, A. E.; Decker, M.; Fofang, N. T.; Liu, S.; Gonzales, E.; Dominguez, J.; Luk, T. S.; Neshev, D. N.; Brener, I.; Kivshar, Y. Tailoring Directional Scattering through Magnetic and Electric Resonances in Subwavelength Silicon Nanodisks. *ACS Nano* **2013**, *7* (9), 7824−7832.

https://dx.doi.org/10.1021/acs.nanolett.0c03744
Nano Lett. 2021, 21, 367−374

(30) Frisk Kockum, A.; Miranowicz, A.; De Liberato, S.; Savasta, S.; Nori, F. Ultrastrong Coupling between Light and Matter. *Nature Reviews Physics* **2019**, *1* (1), 19−40.
(31) Todorov, Y.; Andrews, A. M.; Sagnes, I.; Colombelli, R.; Klang, P.; Strasser, G.; Sirtori, C. Strong Light-Matter Coupling in Subwavelength Metal-Dielectric Microcavities at Terahertz Frequencies. *Phys. Rev. Lett.* **2009**, *102*, 186402.
(32) Todorov, Y.; Andrews, A. M.; Colombelli, R.; De Liberato, S.; Ciuti, C.; Klang, P.; Strasser, G.; Sirtori, C. Ultrastrong Light-Matter Coupling Regime with Polariton Dots. *Phys. Rev. Lett.* **2010**, *105*, 196402.
(33) Ramsteiner, M.; Ralston, J. D.; Koidl, P.; Dischler, B.; Biebl, H.; Wagner, J.; Ennen, H. Doping Density Dependence of Intersubband Transitions in GaAs/Al x Ga1− x As Quantum-Well Structures. *J. Appl. Phys.* **1990**, *67* (8), 3900−3903.
(34) Shtrichman, I.; Metzner, C.; Ehrenfreund, E.; Gershoni, D.; Maranowski, K. D.; Gossard, A. C. Depolarization Shift of the Intersubband Resonance in a Quantum Well with an Electron-Hole Plasma. *Phys. Rev. B: Condens. Matter Mater. Phys.* **2001**, *65* (3), No. 035310.

https://dx.doi.org/10.1021/acs.nanolett.0c03744
Nano Lett. 2021, 21, 367−374